Research Article Vol. 14, No. 7 / 1 Jul 2024 / Optical Materials Express 1793
Optical Materials EXPRESS

Spectroscopy of substrate thermal vibrational modes using an optomechanical sensor

K. G. Scheuer,[1,2] F. B. Romero,[1] and R. G. DeCorby[1,*]

[1]ECE Department, University of Alberta, 9211-116 St. NW, Edmonton, AB T6 G 1H9, Canada
[2]Ultracoustics Technologies Ltd., Sherwood Park, AB T8A 3H5, Canada
[*]rdecorby@ualberta.ca

Abstract: We used an optomechanical sensor to record the vibrational spectrum of its own fused silica substrate. The coupling of the substrate modes was greatly enhanced by covering the sensor with an appropriately sized ethylene glycol droplet, and in that case even thermally populated modes could be clearly detected. We observed a rich spectrum of high-quality flexural modes for frequencies less than ~ 10 MHz, in good agreement with analytical theory and finite element simulations. We also observed signatures of acoustic waves resonantly confined by the droplet, over the entire ~ 0–40 MHz range of the experiment. This work could inform efforts to increase the quality factor of mechanical resonators, and the use of substrate phonon modes as information channels.

1. Introduction and background

It is well-known that the noise generated by an acoustic sensor contains information about its environment [1,2]. In simple terms, this is possible because the (environmental) acoustic boundary conditions are imprinted on the 'random' pressure fluctuations of the medium attached to the sensor. Furthermore, this 'medium noise' can be a significant portion of the overall noise recorded by a sufficiently sensitive detector. This concept has been applied mainly to the study of the earth's crust using the noise recorded by a network of seismic sensors [3]. Nevertheless, the general principle has also been confirmed at high ultrasound frequencies for a sensor attached to a solid metal block [1] or plate [4], or to a column of water [5].

For the sensors used in most previous experiments [1,2,4,5], significant signal processing was required to isolate the 'medium fluctuation' noise embedded within a predominately electrical noise background. Optomechanical ultrasound sensors [6], on the other hand, can readily operate in a thermomechanical-noise-limited regime [7]. Moreover, some devices operate near the limit imposed by the ambient-medium noise [8], making them ideal candidates for passive interrogation of their acoustic environments. We recently reported the use of an optomechanical sensor to probe the acoustic modes of droplets [9,10] and bubbles [11]. Here, we show that these sensors can also be used to record the vibrational spectra of their own underlying substrates. These results have implications for mitigating loss in high-quality, on-chip mechanical resonators [12,13], and also for the study of substrate acoustic modes as information channels [14].

2. Optomechanical sensors

The optomechanical sensors used here are 100-μm-diameter buckled-dome Fabry-Perot cavities, described in detail elsewhere [9–11,15] (see the Supplement 1 file for additional details) and depicted in Fig. 1(a). These devices host high-quality ($Q \sim 10^4$) Laguerre-Gaussian optical modes, and their flexible (buckled) upper mirror plays the role of a high-quality ($Q \sim 10^2$ in air) mechanical oscillator. Thus, they function as optomechanical sensors whose displacement sensitivity ($\sim 10^{-17}$ m/Hz$^{1/2}$) [15] is within 1-2 orders of magnitude of the best-reported values [6]. A typical noise spectrum, for a chip loosely mounted on a stage platform and with an air

#527643 https://doi.org/10.1364/OME.527643
Journal © 2024 Received 16 Apr 2024; revised 4 Jun 2024; accepted 4 Jun 2024; published 12 Jun 2024

Optical Materials EXPRESS

ambient medium, is shown in Fig. 1(b). To capture this data, a low-noise laser was slightly detuned from a fundamental optical resonance of the cavity (*i.e.*, the 'tuned-to-slope' technique), and reflected light was delivered to a broadband photodetector via a circulator. The noise spectrum is dominated by 5 resonant features at ~ 2.5, 6, 12.4, 22.5, and 34.5 MHz, which correspond to the lowest-order radially symmetric vibrational modes of the buckled mirror [9], and for which displacement mode-fields are depicted in the inset figures. The predominance of these modes is due to their near-unity overlap with the optical mode-field (*i.e.,* a fundamental Gaussian beam with spot size ~ 5 µm [15]) used to interrogate the cavity. Lower-magnitude peaks at ~2.8, 8, 17, 28, 31, and 38.5 MHz are due to non-centrosymmetric vibrational modes having a nodal line at the cavity center, and thus exhibiting a much lower overlap factor with the optical mode as detailed in our previous work (see *e.g.*, [15]). The present study is mainly concerned with a set of low-amplitude, higher-quality peaks visible in the ~ 20 kHz to ~ 5 MHz range in Fig. 1(b) and highlighted by the dotted inset box. These correspond to vibrational resonances of the fused silica chip on which the sensors were fabricated. They can easily be suppressed, for example by taping or gluing the chip to a plate, as routinely done in our previous work. Here, our goal was instead to specifically study these substrate acoustic modes, either by actively driving them or by increasing their coupling to the embedded buckled dome sensors.

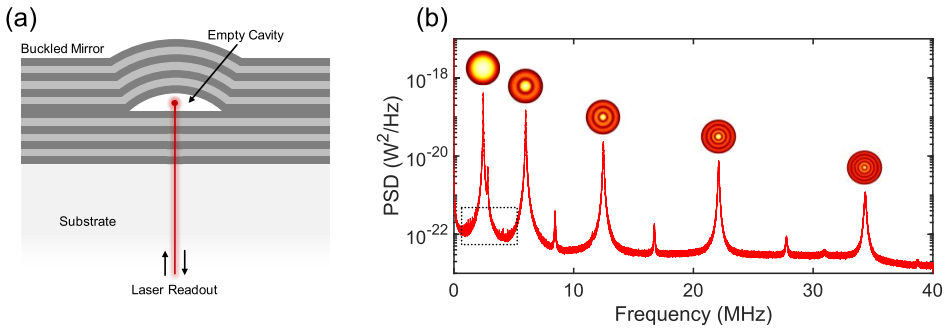

Fig. 1. (a) Schematic depiction of a circular buckled dome optomechanical sensor in cross-section. The aspect ratio is exaggerated for illustration purposes; for the 100-µm-base-diameter domes discussed here, typical peak height is ~ 2 µm, such that an interrogation laser in the 1550 nm wavelength range is coupled to a low-order (m ~ 3) longitudinal resonance. (b) Typical noise spectrum for a sensor in air and with its chip mounted loosely on a stage. The spectrum is dominated by mechanical-thermal noise associated with the radially symmetric vibrational resonances of the buckled mirror, as confirmed by COMSOL simulations. The inset figures show the predicted displacement-mode-field profiles of the 5 lowest-order centrosymmetric modes next to their associated resonance frequency. The dotted-line inset box highlights a collection of weakly coupled substrate vibrational modes, which are the main focus of the present study.

For frequencies above a few hundred kHz, the noise spectrum shown in Fig. 1(b) has two main sources: (i) the mechanical-thermal noise of the oscillator [16] (*i.e.,* the buckled mirror in our case) and (ii) the nearly white noise of the photodetector receiver. The power spectral density (in units of W^2/Hz) of the total noise can be expressed as $S_{PP}(f) = S_{PP}{}^{W} + \alpha \cdot S_{XX}{}^{M}(f)$ [9,17,18], where $S_{PP}{}^{W}$ is the background white noise, $S_{XX}{}^{M}(f)$ is the mechanical-thermal displacement noise (in units of m^2/Hz), and α is a factor (in units of W^2/m^2) quantifying the change in received optical power for a change in the mechanical oscillator position. For frequencies near and below the fundamental mechanical resonance, a single-harmonic oscillator model is often used to model the displacement noise [6] and in the low-frequency limit this predicts a displacement sensitivity

Optical Materials EXPRESS

given by [17]:

$$S_{XX}{}^{M}(0) \approx \frac{k_B T}{2\pi^3 m_0 Q_0 f_0^3} = \frac{4k_B T}{m_0 Q_0 \omega_0^3}, \quad (1)$$

where m_0, Q_0, and f_0 are the effective mass, quality factor, and resonant frequency of the mechanical oscillator. For the buckled domes used here, $m_0 \sim 25$ ng, $Q_0 \sim 100$, and $f_0 \sim 2.5$ MHz [9,15], yielding $S_X{}^{M}(0) = (S_{XX}{}^{M}(0))^{1/2} \sim 4 \times 10^{-17}$ m/Hz$^{1/2}$ at room temperature. The single oscillator model also predicts $S_{XX}{}^{M}(f_0) \sim Q_0{}^2 \cdot S_{XX}{}^{M}(0)$ [6]. However, because the resonant response of the oscillator to an external force (*e.g.,* due to acceleration, or pressure, *etc.*) is enhanced by the same factor, the noise-equivalent signal level is nearly flat versus frequency for an optomechanical sensor operating in a thermomechanical noise limited regime [6,7,15].

For our sensors, as discussed above, there is a near-unity overlap between the dominant mechanical vibrational modes and the optical mode. Thus, the conversion factor is well approximated as $\alpha \sim (P_0 \cdot S \cdot G_\lambda)^2$ [18], where P_0 is the average power received by the photodetector, $S = dR/d\lambda$ is the change in power reflected by the cavity for a change in resonant wavelength, and $G_\lambda = d\lambda/dx$ is the change in resonant wavelength per displacement of the buckled mirror. For a Fabry-Perot cavity, $G_\lambda \sim 2/m$ and $S \sim 1.3/\Delta\lambda$ (*i.e.*, assuming the interrogation laser is tuned to the maximum slope point of the Lorentzian line-shape) [9,15]. For the cavities used here, $m = 3$ and the linewidth is $\Delta\lambda \sim 0.2$ nm, yielding $G_\lambda \sim 0.67$ and $S \sim 6.5 \times 10^9$ m^{-1}. For typical interrogation powers $P_0 \sim 50$ μW, this results in $\alpha \sim 5 \times 10^{10}$ W^2/m^2. Furthermore, the background white noise spectrum is typically dominated by laser shot noise, and thus $S_{PP}{}^{W} \sim 2h\nu P_0/\eta$, where ν is the laser frequency and η is the quantum efficiency of the photodetector. It follows that the shot noise referenced to displacement is given by $S_{XX}{}^{W} = S_{PP}{}^{W}/\alpha \sim 2h\nu/(P_0 \cdot S^2 \cdot G_\lambda{}^2)$. For an optomechanical sensor at non-zero temperature, the best-case sensitivity is achieved by operating in a thermomechanical-noise-limited regime [6,7,15]. This can be achieved by increasing the laser interrogation power within limits set by thermal instabilities and radiation-pressure back-action noise [19]. We typically achieve $S_{XX}{}^{W} < S_{XX}{}^{M}(0)$ with P_0 in the 10–100 μW range for our sensors operating in air, well below the threshold for thermal instabilities or significant radiation-pressure effects. Of course, our device sensitivity also lies several orders of magnitude above the standard quantum limit (SQL) for displacement sensitivity in the absence of thermal noise, given by $S_{XX}{}^{SQL}(\omega_0) \sim 2 \cdot \hbar \cdot Q_0/(m_0 \cdot \omega_0{}^2)$ [20,21], and which yields $S_X{}^{SQL}(\omega_0) \sim 10^{-18}$ m/Hz$^{1/2}$ (*i.e.*, $S_X{}^{SQL}(0) \sim 10^{-20}$ m/Hz$^{1/2}$) for our devices by assuming the same value for Q_0 as above (*i.e.*, neglecting back-action effects [19]).

3. Substrate (plate) vibrational modes

The sensors studied here were part of a large sensor array, on a fused silica chip diced from a larger substrate (Corning HPFS 7980) with nominal thickness of 500 μm. Multiple chips were studied and produced similar results, but we focus the discussion below on a particular chip having lateral dimensions of ~ 9.6 mm × 9.6 mm. For the measurements described here, the chip was loosely placed on an aluminum plate attached to a micro-positioner, and aligned to a small hole in the plate which provided optical access from beneath the chip. All measurements were performed in ambient laboratory conditions. The supporting plate was not particularly smooth, and the interface between the plate and the chip is expected to contain many air pockets, such that the acoustic coupling is relatively weak [13]. Thus, we treat the chip as a square plate with completely free boundary conditions, also ignoring any perturbations caused by the thin film sensors fabricated on the top surface. The vibrational modes of such a plate, while mathematically challenging [22], are well-known. They have eigen-frequencies which can be expressed as $f_{mn} = \Lambda(D/\rho h)^{1/2}/a^2$, where $D = Eh^3/[12(1\text{-}\nu^2)]$ is the flexural rigidity, E is the Young's modulus, ν is Poisson's ratio, ρ is the mass density, and h and a are the thickness and side-length of the plate, respectively. For the fused silica substrate studied here, $h \sim 500$ μm, $a \sim 0.96$ cm, $\rho \sim 2200$ kg/m^3, $E \sim 73$ GPa, and $\nu \sim 0.16$. Furthermore, the mode-dependent pre-factor has values

Optical Materials EXPRESS

given by $\Lambda \approx 13.5, 19.6, 24.3, 34.8, 61.1, 63.7\ldots$ for the lowest-order modes of the square plate with free boundaries [23,24]. It should be mentioned that these solutions assume $\nu = 0.3$, while $\nu \sim 0.16$ is more typical for the fused silica plates of interest here. This is expected to cause only slight discrepancies in the predicted eigen-frequencies, as supported by close agreement with the numerical (COMSOL) results (see the SI file).

The mode with the lowest resonant frequency is a 'torsional mode' [22], characterized by opposite corners of the square plate moving in common phase and a single nodal line running centrally along each transverse direction (*i.e.*, $m = n = 1$). A mode-field amplitude plot for this mode, obtained using COMSOL, is shown in the inset of Fig. 2(a). Both the analytical result above and the numerical solver predict $f_{11} \sim 20$ kHz for our chip of interest. It is interesting to estimate the displacement amplitude of these substrate vibrational modes using Eq. (1), which is derived from the equipartition theorem [16,17]. Assuming $m_0 \sim 0.25 \cdot m_{\text{plate}}$ (*i.e.*, the modal effective mass for a square plate or membrane [17]) ~ 22 mg, $Q_0 \sim 10^3$ (see below), and $f_0 \sim 50$ kHz (*i.e.,* one of the lowest-order mode frequencies), we estimate $S_{XX}{}^{\text{plate}}(f_0) \sim Q_0 k_B T/(2\pi\,{}^3 m_0 f_0{}^3)$, or $S_X{}^{\text{plate}}(f_0) \sim 5 \times 10^{-15}$ m/Hz$^{1/2}$, which is two orders of magnitude above the displacement sensitivity noise floor of the sensor described above. However, the amplitude of these features in the sensor noise spectrum will also depend on the coupling between the substrate vibrations and the displacement of the sensor's buckled mirror (*i.e.,* the latter of which is read out by the laser). For the sensors in air, we speculate that this might occur via a coupling between in-plane strain and the height of the buckled mirror, as discussed in our previous work [25]. In any case, the coupling is apparently quite weak since these modes lie only slightly above the noise floor (see Fig. 1(b)).

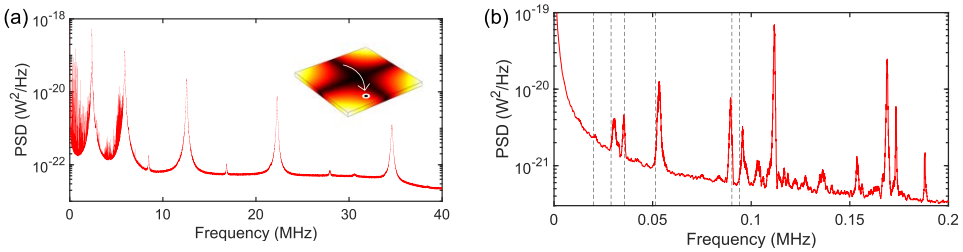

Fig. 2. (a) Spectrum recorded for the same sensor as in Fig. 1(b), but with vibrational energy supplied via a piezoelectric transducer (1.5 MHz center frequency) attached to the aluminum plate on which the chip is loosely mounted. The inset figure depicts the mode-field amplitude profile as predicted by COMSOL for the lowest-frequency vibrational mode of the ~ 0.96 cm x 0.96 cm square, fused silica chip described in the main text. The predicted eigen-frequency for this mode is ~ 20 kHz. The location of the sensor on the chip, and its relative size, is also shown schematically. (b) The low-frequency portion of the spectrum is plotted alongside the 6 lowest-order, analytically predicted eigen-frequencies (dashed vertical lines) for the chip. The lowest-order mode at ~ 20 kHz is barely visible here but was confirmed more confidently from the droplet-covered-sensor measurements below. Note also that the active driving process broadens these resonant features relative to their intrinsic linewidth (see main text).

To increase the amplitude of the substrate vibrations, we attached a piezo transducer to the aluminum plate on which the chip was resting (various transducers were used, see the SI file for details). This enabled the sensor to resolve vibrational features over a wide frequency range extending up to nearly 10 MHz and including the region below a few hundred kHz where laser and $1/f$ noise are significant. This furthermore enabled us to compare the experimentally observed resonances to the analytical (and COMSOL numerical) predictions for the lowest-order vibrational eigen-frequencies of the square substrate. An example result is shown in Fig. 2(b),

Optical Materials EXPRESS

revealing excellent agreement for the first 6 eigen-frequencies. The lowest-order mode at ~ 20 kHz is only barely visible here but was observed as a stronger feature for droplet-covered sensors (below). Furthermore, from data collected using multiple sensors on the same chip, and under varying conditions (*i.e.,* sensor in air or covered by liquid), we found that the location of these resonant features was unchanged, supporting the conclusion that they are modes of the substrate itself and not of an individual sensor or droplet. Notably, the relative amplitude of these features does vary between sensors, which is expected since the coupling between a given substrate mode and a given sensor would depend greatly on the location of the sensor on the chip [13], as depicted in the inset of Fig. 2(a). It should also be noted that the resonant features in Fig. 2(b) are broadened relative to their native linewidths (see Fig. 5 below). This is because the pulsed energy delivered by the piezo transducer effectively modulates the substrate modes at the pulse repetition rate (200 Hz here), producing sidebands on each of the substrate modes. Further explanation is provided in the SI file.

4. Droplet-enhanced readout of substrate vibrations

For the substrate vibrational modes to manifest as features in the spectrum of the optomechanical sensor, their energy must somehow be coupled to variations in the height of the sensor cavity. Changes in the in-plane strain, for example with temperature due to thermal expansion mismatch, are known to drive vertical deflections of our buckled-dome cavities [25]. We speculate that this is in fact the dominant coupling mechanism for the sensors in air described above; *i.e.,* flexural lamb-wave modes of the square substrate produce localized bending of the chip near a sensor of interest, which in turn modifies the stress/strain of the buckled mirror and thus modulates the cavity height.

A greatly enhanced coupling of substrate modes was made possible by depositing a droplet (ethylene glycol, EG) over the region containing the sensor of interest, as shown in Fig. 3(a). It is important to note that the droplets used here were much larger than the micron-scale droplets from our previous work [9,10]. Rather, the droplets discussed in the following, while varying in size and shape, typically had a base diameter of several millimeters (see Fig. 1(a)) and a shallow, puddle-like profile. As shown below, this type of droplet combined with the loose mounting mentioned above resulted in strong signatures of the substrate vibrational modes appearing in the noise floor of the sensors.

Coupling of substrate acoustic waves to sessile droplets is a widely studied topic in the field of 'acoustofluidics' [26], motivated by the potential to use ultrasonic actuators to drive processes such as translation or jetting-based-breakup of droplets, or for mixing or streaming-based concentration, separation or patterning of suspended particles [27]. While much of this work has used surface acoustic waves (SAWs), flexural Lamb wave modes have also been employed [27–29]. The basic mechanism is depicted in Fig. 3(b) and is briefly summarized as follows. An acoustic mode (surface or bulk waves) which would normally be confined to the substrate becomes leaky in the region adjacent to the droplet, and some of its energy is converted to a compressional (*i.e.*, longitudinal acoustic) wave inside the liquid. For a flexural Lamb wave in the substrate, the compressional wave is radiated into the liquid at a refraction angle given by $\theta_L = \sin^{-1}(c_{liquid}/c_{Lamb})$ [28], where c_{liquid} is the sound velocity in the liquid and c_{Lamb} is the phase velocity of the Lamb wave. The sound energy radiated into the droplet is highly confined by impedance-mismatch at the air and substrate boundaries and can thus be detected by the optomechanical sensor embedded within. The droplets used here are very similar in size (*e.g.*, ~ 1-3 mm base diameter) to those employed in the cited works [26–29], lending credence to the proposed coupling mechanism. Notably, the coupling of the substrate modes to the sensor was observed to be weaker for droplets smaller than ~ 1 mm [9,10], while droplets larger than ~ 3 mm resulted in significant damping of the substrate modes (see below).

Optical Materials EXPRESS

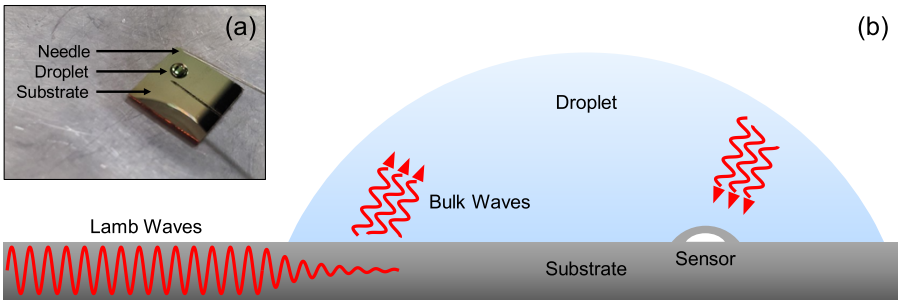

Fig. 3. (a) A photograph showing a typical EG droplet lying over a particular sensor, which is optically interrogated from below. The chip has side length ~ 9.6 mm and contains hundreds of individual sensors which are not visible at this scale. The droplet shown has base diameter ~ 2 mm and height ~ 0.5 mm. (b) A schematic depiction of the proposed mechanism for enhanced coupling between the substrate modes and the optomechanical sensor. Flexural Lamb wave modes in the substrate become leaky adjacent to the droplet, and couple to longitudinal compressive waves inside the liquid. These longitudinal waves are strongly confined to the droplet, due to impedance mismatch at the air and substrate boundaries and are thus imprinted as incoming pressure waves on the sensor of interest.

Now, it is important to also note that the droplet hosts its own acoustic resonant modes. In fact, in our previous work [9,10] we specifically studied those modes by centering smaller (sub-millimeter-scale) sessile droplets on one of our sensors. Here, larger droplets are employed and, while they are deposited over the sensor to be interrogated, they are intentionally not centered with respect to that sensor (several representative images are provided in the SI file). Nevertheless, these droplets can be viewed as mechanical oscillators (or alternatively as acoustic resonators) in their own right. In fact, the experiment depicted in Fig. 3(b) can be viewed as a system of three interacting mechanical/vibrational resonators: the substrate, the droplet, and the embedded optomechanical sensor (*i.e.,* its flexible buckled mirror). Not surprisingly, the resulting noise spectra (with the sensor operating in the thermomechanical-noise-limited regime) are quite complex, containing a myriad array of Fano resonance features consistent with coupled harmonic oscillators [9].

To gain some high-level insight into the origin of these features, we captured noise spectra under varying conditions as shown in Fig. 4. First, we completely covered a chip in a large quantity of EG, so that the noise spectrum (see Figs. 4(a) and (b)) is representative of the sensor embedded in a 'bulk' EG half-space medium. As explained elsewhere [15], the spectrum is dominated by the same signatures of the centro-symmetric vibrational modes of the buckled mirror as discussed for the air case above, but broadened and shifted to lower frequencies (*i.e.*, here at ~ 0.7, 3, 7, 13, 22, and 33 MHz) due to the 'added mass' and viscous damping associated with the EG medium [9]. In this case, the spectrum is mostly 'smooth' and devoid of resonant features associated with the sensor's surrounding environment. Notably, this large quantity of EG effectively dampens the substrate vibrational modes, although some weak features are still discernible in the ~ 1 - 2 MHz range. Next, we conducted an experiment in which the chip was floated on a layer of water (between the substrate and the aluminum plate) and with the sensor of interest covered by a mm-scale EG droplet of the type described above. In this case, the sensor noise spectrum (see Figs. 4(c) and (d)) exhibits the same underlying vibrational spectrum as in part (a), but augmented by a collection of moderate quality (Q ~ 10 - 100), Fano-like resonant features. These can be attributed to the bulk acoustic modes of the droplet [9,10], as established in our previous works. They emerge at lower frequencies here (*e.g.*, see the first feature at ~ 350 kHz in Fig. 4(d)) due to the larger size of the droplets. Remarkably, signatures of droplet

Optical Materials EXPRESS

acoustics were visible over the entire frequency range of our sensor, often manifesting as equally spaced 'fringes' in the ~ 5–40 MHz range. These fringes are only weakly visible in Fig. 4(c) but are much more obvious in datasets provided below and in the SI file. The frequency spacing of the fringes was observed to be inversely related to the droplet size (especially height), and we speculate that they might arise from reverberations between the buckled mirror and the surface of the droplet [1,5]. It is worth noting that droplets can also support surface-tension-mediated capillary modes. However, these typically manifest at much lower frequencies than the features discussed above [9].

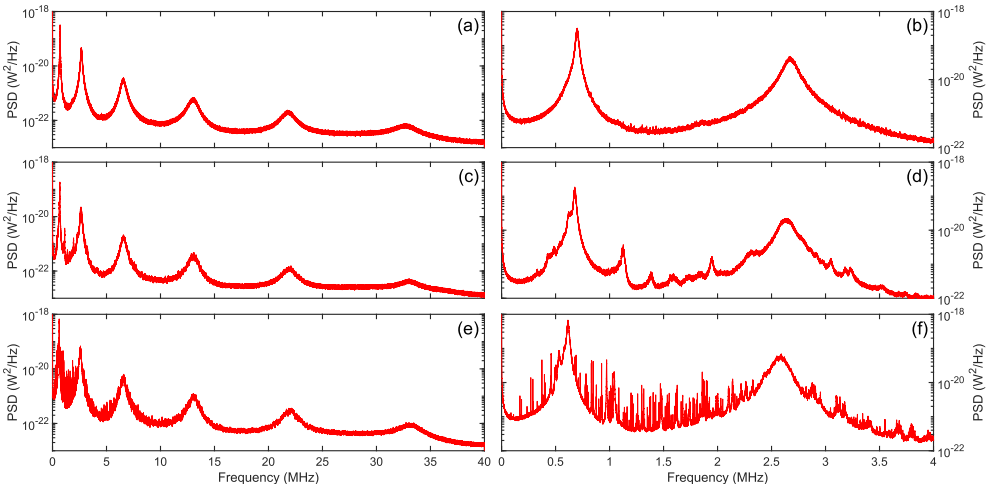

Fig. 4. Thermo-mechanical noise spectra captured for 3 different, but nominally identical sensors covered by ethylene glycol (EG). (a,b) Sensor covered by a large quantity of EG, thus approximating a 'bulk' EG half-space above the sensor. (c,d) Sensor covered by a mm-scale EG droplet, and with the sensor chip 'floating' on a layer of water to dampen the substrate vibrational modes. The Fano-like resonance features ($Q < 10^2$) present on the background (sensor) spectrum are attributable to the resonant acoustic modes of the droplet. (e,f) Sensor covered by a mm-scale droplet and with the sensor chip loosely mounted on an aluminum plate. In this case, narrow linewidth resonance features ($Q > 10^3$) are present in addition to the sensor and droplet resonances, and can be attributed to the vibrational modes of the fused silica chip.

Finally, Figs. 4(e) and (f) show a spectrum obtained with a similarly sized droplet on top of a sensor, but with the chip resting freely on the aluminum plate below. In this case, both the native dome resonances and the droplet Fano-like features are still present, but an additional set of higher quality ($Q \sim 10^3$-10^4) features emerges. As with the air-medium results in Section 2, we verified that the frequencies of these features are consistent with those expected for the vibrational modes of the fused silica chip. Notably, these thermally driven substrate modes lie ~ 1 - 2 orders of magnitude above the sensor noise floor, consistent with the analysis above. This furthermore indicates that the droplet enables a highly efficient coupling of the flexural Lamb modes of the substrate to the optomechanical sensor.

A second thermomechanical noise spectrum, for a different sensor/droplet combination is shown in Fig. 5(a). Note that the 'fringes' above ~ 5 MHz are more visible in this case. A portion of this spectrum, plotted on a linear scale, is shown in Fig. 5(b). Per the arguments above, the individual peaks correspond to particular vibrational modes of the underlying chip. They exhibit $Q > 10^3$, in very good agreement with the results reported by de Jong *et al.* [13] for a fused silica chip of very similar size and shape, and obtained in that case using a laser Doppler

Optical Materials EXPRESS

vibrometer (LDV). Note that fused silica can support mechanical modes having $Q > 10^6$ [30], but that requires the sample to be in vacuum and mechanically isolated from its supports. Here, the Q-factor is undoubtedly limited by air damping and by phonon radiation into the supporting aluminum plate. Some of the modes barely lie above the noise floor, and undoubtedly the modes observed are only a fraction of those supported by the substrate. The number of substrate modes observed, and the associated SNR, was higher for certain droplet/sensor combinations (see SI file for several examples). To resolve a higher number of these modes, we actively drove the supporting plate with a piezo transducer as described in Section 3. A typical result obtained using a transducer centered at 4 MHz is shown in Fig. 5(c), and exhibits a dense collection of substrate modes extending up to ~ 10 MHz. We wrote a script to count these modes over the 0–4 MHz frequency range, and compared this to the number of modes predicted by a COMSOL simulation of a fused silica slab with the same dimensions as the chip. The results are shown in Fig. 5(d), in the form of a bar graph indicating the number of modes in 0.1-MHz-wide bins. The overall agreement is reasonable, although as might be expected the experiment does not capture every mode. This is likely due to some modes having a node at the position of the particular sensor used [13]. Also, the discrepancy seems to be highest near the resonant features of the optomechanical sensor, which might indicate that mode hybridization in those regions makes it difficult to identify the substrate modes as independent entities.

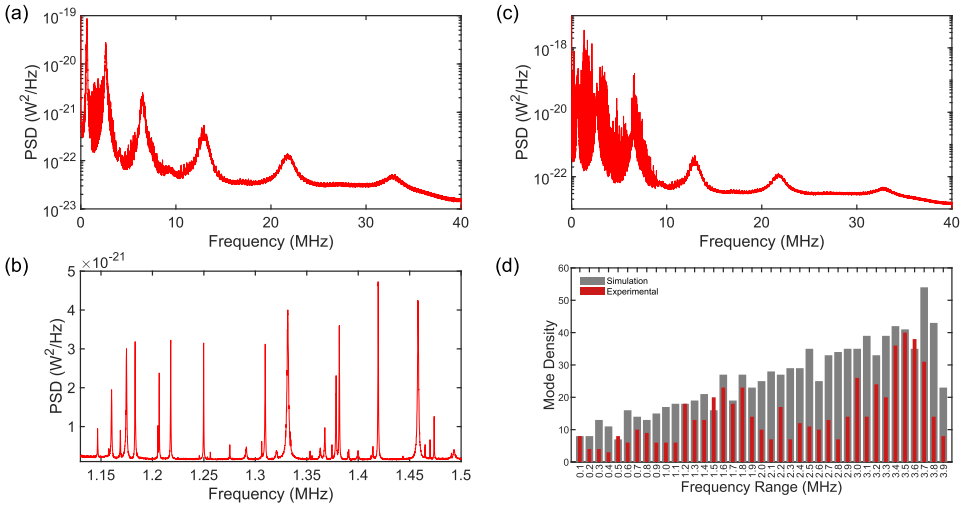

Fig. 5. (a) Typical noise spectrum for a droplet-covered sensor on a loosely mounted chip. (b) Zoomed-in portion of the curve in part a., showing substrate vibrational modes in greater detail. Most of the modes exhibit $10^3 < Q < 10^4$. (c) Noise spectrum for the same droplet-covered sensor as in part a., but with a piezoelectric transducer actively driving the aluminum plate on which the sensor chip sits. (d) Bar chart indicating the number of modes in fixed frequency intervals extracted from the data in part c., compared to the number of modes extracted from a COMSOL simulation of a fused silica plate having the same dimensions as the sensor chip.

5. Discussion and conclusions

Our results demonstrate the unique ability of optomechanical sensors to record the thermally driven motions of their surroundings. This is possible because optomechanical sensors can routinely be made to operate in a regime where their noise floor and quality factor is substantially set by ambient-medium noise. The 'fluctuation-dissipation' theorem [16] requires that the flow

Optical Materials EXPRESS

of energy between the 'environment' and the mechanical oscillator is bi-directional and balanced at thermal equilibrium. Thus, any thermal motion in the environment will be imprinted (via a 'thermal Langevin' source [31]) on the motion of the oscillator. If the environment has boundary conditions which impart resonant modes on this thermal motion, such as for the droplets and substrate chips studied here, that structure will in turn be imprinted on the noise floor of the sensor. These concepts are well-known [1,3–5], but emerge more readily with optomechanical sensors because electrical noise can be effectively eliminated.

The observation and study of substrate vibrational modes, and their impact on embedded devices, has implications for several emerging applications. For example, high-quality mechanical resonators are of great interest for sensing and quantum information science [6,31], and a higher Q-factor is associated with improved sensitivity and higher coherence. State-of-the-art resonators are constructed from materials such as silicon nitride or diamond with low intrinsic loss, and typically operate in vacuum to minimize viscous damping and acoustic radiation losses [31]. In such cases, the residual loss is often dominated by the thermal coupling between the resonator element and its underlying support substrate (*e.g.*, a chip or frame), motivating the development of sophisticated techniques for minimizing this coupling [32–35]. Some of these same techniques, including the use of soft-clamping [33] and phononic bandgap isolation [35], have potential to increase the mechanical quality of our buckled-dome cavities and could be explored in future work.

While the substrate has often been treated as a thermal bath of infinite extent [36], the finite size of a practical chip implies the possibility for coherent exchange of phonons between an embedded mechanical oscillator and the vibrational modes of the underlying substrate [12]. For example, De Jong *et al.* [13] recently showed that substrate resonant modes can impact the spectrally dependent quality factor of an embedded high-Q membrane and also mediate long-range interactions between multiple membrane oscillators in an array. Aside from these parasitic effects, substrate acoustic modes have the potential to be exploited as channels for the coherent transfer of phonons between individual devices [14].

In summary, we have shown that an on-chip optomechanical sensor can be used to interrogate the vibrational resonances of its own substrate, and that covering the sensor with an appropriately sized droplet enables a significantly enhanced detection of these modes. The results demonstrate the unique capabilities of optomechanical sensors to detect thermal vibrations in their environment, and might also inform future efforts to mitigate the impact of substrate modes as loss channels for embedded oscillators or to exploit substrate modes as channels for coherent transfer of phonons.

Funding. Government of Alberta (Innovation Catalyst Grant); Mitacs (Accelerate IT38340); Natural Sciences and Engineering Research Council of Canada (Discovery Grants Program).

Acknowledgements. We thank Graham Hornig for assistance with experiments, and for useful discussions.

Disclosures. Ultracoustics Technologies Ltd. (E,P) KGS, (P,S) RGD.

Data availability. Data underlying the results presented in this paper are not publicly available at this time but may be obtained from the authors upon reasonable request.

Supplemental document. See Supplement 1 for supporting content.

References

1. R. L. Weaver and O. I. Lobkis, "Ultrasonics without a source: thermal fluctuation correlations at MHz frequencies," Phys. Rev. Lett. **87**(13), 134301 (2001).
2. N. M. Shapiro, M. Campillo, L. Stehly, *et al.*, "High-resolution surface-wave tomography from ambient seismic noise," Science **307**(5715), 1615–1618 (2005).
3. R. Snieder and K. Wapenaar, "Imaging with ambient noise," Phys. Today **63**(9), 44–49 (2010).
4. V. Loyau and G. Feuillard, "Relationship between electrical impedance of a transducer and its electroacoustic behavior: measurement without a primary source," J. Appl. Phys. **100**(3), 034909 (2006).
5. S. Lani, S. Satir, G. Gurun, *et al.*, "High frequency ultrasonic imaging using thermal mechanical noise recorded on capacitive micromachined transducer arrays," Appl. Phys. Lett. **99**(22), 224103 (2011).
6. B.-B. Li, L. Ou, Y. Lei, *et al.*, "Cavity optomechanical sensing," Nanophotonics **10**(11), 2799–2832 (2021).

Optical Materials EXPRESS

7. F. Zhou, Y. Bao, R. Madugani, *et al.*, "Broadband thermomechanically limited sensing with an optomechanical accelerometer," Optica **8**(3), 350–356 (2021).
8. S. Basiri-Esfahani, A. Armin, S. Forstner, *et al.*, "Precision ultrasound sensing on a chip," Nat. Commun. **10**(1), 132 (2019).
9. G. J. Hornig, K. G. Scheuer, and R. G. DeCorby, "Observation of thermal acoustic modes of a droplet coupled to an optomechanical sensor," Appl. Phys. Lett. **123**(4), 042202 (2023).
10. K. G. Scheuer, F. B. Romero, G. J. Hornig, *et al.*, "Ultrasonic spectroscopy of sessile droplets coupled to optomechanical sensors," Lab Chip **23**(24), 5131–5138 (2023).
11. K. G. Scheuer, F. B. Romero, and R. G. DeCorby, "Observation of thermal acoustic breathing modes of a bubble," arXiv, arXiv:2308.01989v2. (2023).
12. A. Jockel, M. T. Rakher, M. Korppi, *et al.*, "Spectroscopy of mechanical dissipation in micro-mechanical membranes," Appl. Phys. Lett. **99**(14), 143109 (2011).
13. M. H. J. de Jong, M. A. ten Wolde, A. Cupertino, *et al.*, "Mechanical dissipation by substrate-mode coupling in SiN resonators," Appl. Phys. Lett. **121**(3), 032201 (2022).
14. R. Singh and T. P. Purdy, "Detecting acoustic blackbody radiation with an optomechanical antenna," Phys. Rev. Lett. **125**(12), 120603 (2020).
15. G. J. Hornig, K. G. Scheuer, E. B. Dew, *et al.*, "Ultrasound sensing at thermomechanical limits with optomechanical buckled-dome microcavities," Opt. Express **30**(18), 33083–33096 (2022).
16. T. B. Gabrielson, "Mechanical-thermal noise in micromachined acoustic and vibration sensors," IEEE Trans. Electron Dev. **40**(5), 903–909 (1993).
17. B. D. Hauer, C. Doolin, K. S. D. Beach, *et al.*, "A general procedure for thermomechanical calibration of nano/micro-mechanical resonators," Ann. Phys. **339**, 181–207 (2013).
18. G. J. Hornig, S. Al-Sumaidae, J. Maldaner, *et al.*, "Monolithically integrated membrane-in-the-middle cavity optomechanical systems," Opt. Express **28**(19), 28113–28125 (2020).
19. T. J. Kippenberg and K. J. Vahala, "Cavity optomechanics: back-action at the mesoscale," Science **321**(5893), 1172–1176 (2008).
20. A. Schliesser, G. Anetsberger, R. Riviere, *et al.*, "High-sensitivity monitoring of micromechanical vibration using optical whispering gallery mode resonators," New J. Phys. **10**(9), 095015 (2008).
21. A. G. Krause, M. Winger, T. D. Blasius, *et al.*, "A high-resolution microchip optomechanical accelerometer," Nat. Photonics **6**(11), 768–772 (2012).
22. T. D. Rossing and D. A. Russell, "Laboratory observation of elastic waves in solids," Am. J. Phys. **58**(12), 1153–1162 (1990).
23. A. W. Leissa, "The free vibration of rectangular plates," J. Sound Vib. **31**(3), 257–293 (1973).
24. Y. Xing, G. Li, and Y. Yuan, "A review of the analytical solution methods for the eigenvalue problems of rectangular plates," Int. J. Mech. Sci. **221**, 107171 (2022).
25. M. H. Bitarafan, H. Ramp, T. W. Allen, *et al.*, "Thermomechanical characterization of on-chip buckled-dome Fabry-Perot microcavities," J. Opt. Soc. Am. B **32**(6), 1214–1220 (2015).
26. W. Connacher, N. Zhang, A. Huang, *et al.*, "Micro/nano acoustofluidics: materials, phenomena, design, devices, and applications," Lab Chip **18**(14), 1952–1996 (2018).
27. A. R. Rezk, L. Y. Yeo, and J. R. Friend, "Poloidal flow and toroidal particle ring formation in a sessile drop driven by meghahertz order vibration," Langmuir **30**(37), 11243–11247 (2014).
28. W. Liang and G. Lindner, "Investigations of droplet movement excited by Lamb waves on a non-piezoelectric substrate," J. Appl. Phys. **114**(4), 044501 (2013).
29. G. Destgeer, B. Ha, J. Park, *et al.*, "Lamb wave-based acoustic radiation force-driven particle ring formation inside a sessile droplet," Anal. Chem. **88**(7), 3976–3981 (2016).
30. W. J. Startin, M. A. Beilby, and P. R. Saulson, "Mechanical quality factors of fused silica resonators," Rev. Sci. Instrum. **69**(10), 3681–3689 (1998).
31. M. Aspelmeyer, T. J. Kippenberg, and F. Marquardt, "Cavity optomechanics," Rev. Mod. Phys. **86**(4), 1391–1452 (2014).
32. R. A. Norte, J. P. Moura, and S. Gröblacher, "Mechanical resonators for quantum optomechanics experiments at room temperature," Phys. Rev. Lett. **116**(14), 147202 (2016).
33. Y. Tsaturyan, A. Barg, E. S. Polzik, *et al.*, "Ultracoherent nanomechanical resonators via soft clamping and dissipation dilution," Nat. Nanotechnol. **12**(8), 776–783 (2017).
34. A. H. Ghadimi, S. A. Fedorov, N. J. Engelsen, *et al.*, "Elastic strain engineering for ultralow mechanical dissipation," Science **360**(6390), 764–768 (2018).
35. G. S. MacCabe, H. Ren, J. Luo, *et al.*, "Nano-acoustic resonator with ultralong phonon lifetime," Science **370**(6518), 840–843 (2020).
36. S. Chakram, Y. S. Patil, L. Chang, *et al.*, "Dissipation in ultrahigh quality factor SiN membrane resonators," Phys. Rev. Lett. **112**(12), 127201 (2014).